Electrodynamic response of the type-II Weyl semimetal YbMnBi_{2}

M. Chinotti, A. Pal, W. J. Ren, C. Petrovic, and L. Degiorgi

Electrodynamic response of type II Weyl semimetal YbMnBi$_2$

M. Chinotti[+], A. Pal[+], and L. Degiorgi[*]

Laboratorium für Festkörperphysik, ETH - Zürich, 8093 Zürich, Switzerland

W.J. Ren

Condensed Matter Physics and Materials Science Department,
Brookhaven National Laboratory, Upton NY 11973, USA and
Shenyang National Laboratory for Materials Science, Institute of Metal Research,
Chinese Academy of Sciences, Shenyang 110016, China

C. Petrovic

Condensed Matter Physics and Materials Science Department,
Brookhaven National Laboratory, Upton NY 11973, USA

(Dated: November 2, 2016)

Weyl fermions play a major role in quantum field theory but have been quite elusive as fundamental particles. Materials based on quasi two-dimensional bismuth layers were recently designed and provide an arena for the study of the interplay between anisotropic Dirac fermions, magnetism and structural changes, allowing the formation of Weyl fermions in condensed matter. Here, we perform an optical investigation of YbMnBi$_2$, a representative type II Weyl semimetal, and contrast its excitation spectrum with the optical response of the more conventional semimetal EuMnBi$_2$. Our comparative study allows us disentangling the optical fingerprints of type II Weyl fermions, but also challenge the present theoretical understanding of their electrodynamic response.

PACS numbers: 71.20.Gj,78.20.-e

Since the discovery of Dirac states in a wide range of materials spanning novel superconductors [1], graphene [2] as well as topological insulators [3], a great deal of effort has been devoted to observe other types of elementary particles in condensed matter, like Majorana and Weyl fermions. The latter type of fermions may be understood as a pair of particles characterized by opposite chirality, as derived by the massless solution of the Dirac equation [4]. In order to observe Weyl fermions in three dimensional condensed matter systems, the requirement of a crossing of two non-degenerate bands, containing relativistic and massless states which just touch in a single point, must be satisfied [5, 6]. Indeed, a split of the doubly degenerate Dirac point into a pair of Weyl nodes can be induced in the presence of broken time reversal or space inversion symmetry [7].

Broken space inversion symmetry at a single Dirac cone leads to two Weyl nodes hallmarked by the same momentum but shifted by the same amount in opposite directions along the energy axis relatively to each other, while broken time-reversal symmetry results in Weyl nodes at the same energy but separated in momentum space [5]. Evidences for Weyl fermions with broken space inversion symmetry have been reported in so-called non-centrosymmetric, transition metal monopnictide crystals, like TaAs and TaP [8, 9]. Moreover, the proposal for the existence of two types of Weyl semimetal was recently made; the standard type I with point-like Fermi surface and the previously overlooked type II arising at the contact of the Fermi level along the line boundaries of electron and hole pockets [10, 11]. A type II Weyl semimetallic state has been predicted [12] and observed

in MoTe$_2$ [13].

The quasi two-dimensional bismuth layers AMnBi$_2$ (A = alkaline as well as rare earth atom) lately advanced as a suitable playground for the investigation of such emergent low-energy quasiparticle excitations [14–17]. These non-centrosymmetric and magnetic materials host strong spin-orbital interaction and their two-dimensional network of Bi atoms guarantees Dirac massless dispersions. Furthermore, the broken time-reversal symmetry lifts the degeneracy at the Dirac cones [18]. EuMnBi$_2$ and YbMnBi$_2$ were thoroughly scrutinized with respect to the electronic properties of Weyl fermions. High precision ARPES investigations show that YbMnBi$_2$ (but not EuMnBi$_2$) is a genuine Weyl semimetal of type II [19].

A variety of representative Dirac and Weyl semimetals, like for instance pyrochlore iridates, quasicrystals and transition metal monopnictides, were recently addressed from the perspective of their optical response [20–25]. Here, we are triggered by the opportunity to exploit YbMnBi$_2$ and EuMnBi$_2$ as an arena in order to explore the optical response and chase the related fingerprints of a type II Weyl semimetal (i.e., in the Yb-based material) in contrast to its semimetal counterpart (i.e., the Eu compound). Our optical experiment provides evidence for two intervals with a linear frequency dependence of the real part ($\sigma_1(\omega)$) of the optical conductivity in the Yb material, with the slope of the low-energy larger than the one of the high-energy interval. Both linear frequency dependences of $\sigma_1(\omega)$ extrapolate to zero conductivity at the origin of the frequency axis. These features together with characteristic van Hove singularities are the major optical signatures of Weyl fermions.

Indeed, in the Eu compound only one linear frequency dependence can be clearly identified at high frequencies, which cuts the frequency axis at a finite value and thus indicates its gapped nature. Our results broadly agree with recent predictions of the optical response in Weyl semimetals [26–28] but equally put novel constraints for future theoretical activities.

Our EuMnBi$_2$ and YbMnBi$_2$ single and well-characterized crystals were grown after the procedure described in Refs. 17 and 29, leading to specimens with shiny surface of typical size 2x2 mm^2. We collect reflectivity spectra ($R(\omega)$) from the far-infrared up to the ultraviolet as a function of temperature [30, 31]. This is the prerequisite in order to perform reliable Kramers-Kronig transformation, giving access to the optical conductivity. To this end, standard and well established extrapolation procedures of $R(\omega)$ are applied at low as well as high frequencies. In the dc limit (i.e., $\omega \rightarrow 0$) we use the Hagen-Rubens (HR) extrapolation of $R(\omega)$ ($R(\omega) = 1 - 2\sqrt{\frac{\omega}{\sigma_{dc}}}$) with dc conductivity ($\sigma_{dc}$) in agreement with the transport values [29].
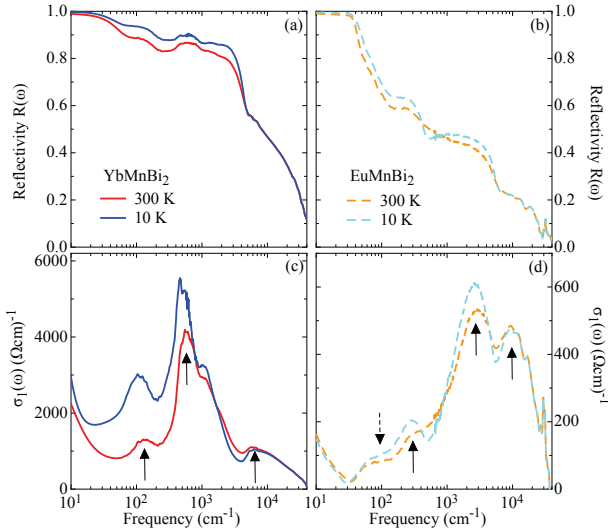

FIG. 1: (color online) (a) and (b) Reflectivity spectra, and (c) and (d) real part $\sigma_1(\omega)$ of the optical conductivity at 300 and 10 K of YbMnBi$_2$ and EuMnBi$_2$, respectively. Please note the logarithmic energy scale in all panels. The arrows emphasize the pronounced absorptions (plain) and shoulder (dashed) in $\sigma_1(\omega)$ (see text).

First of all, we introduce in Fig. 1(a) and (b) the measured $R(\omega)$ spectra at 10 and 300 K for both compounds. While $R(\omega)$ in the Yb material steeply increases in a rather metallic-like fashion upon decreasing the frequency, with a plasma edge feature below 5000 cm^{-1}, $R(\omega)$ of the Eu compound displays a more gradual increase and merges only at the lower frequency limit of our spectrometer into the metallic HR extrapolation.

The corresponding $\sigma_1(\omega)$ is shown in panels (c) and (d) of Fig. 1. The overall optical response shares several common features with the charge dynamics of semimet-

als, like e.g. WTe$_2$ [32]. By first inspecting the spectra at low frequencies, we recognize a metallic contribution merging into a Drude-like resonance well below 100 cm^{-1} at all temperatures, in broad agreement with the dc transport properties of both materials [29]. This bears testimony to a rather small scattering rate (i.e., width of the Drude resonance), so that the metallic component is quite narrow, falling into the spectral range dominated by the HR extrapolation of the measured $R(\omega)$. A narrowing of the Drude resonance has been also encountered in TaAs with decreasing temperature [23]. The overall metallic contribution is however rather weak, particularly in the Eu compound, which suggests small Drude weight and moderate-to-low concentration of itinerant charge carriers. This is consistent with the rather fuzzy signature of the Fermi surface, as measured with ARPES technique [19]. Because of the narrow nature of the Drude resonance in $\sigma_1(\omega)$, it is not realistic to artificially disentangle the related temperature dependence of the Drude parameters, plasma frequency and scattering rate.

Three broad peaks at $\sim$ 100, 500 and 6000 cm^{-1} and at $\sim$ 300, 2500 and 10000 cm^{-1} dominate $\sigma_1(\omega)$ in Yb and Eu compound, respectively (see plain arrows in Fig. 1(c) and (d)). Since the absorptions at 100 and 300 cm^{-1} in the Yb and Eu material, respectively, are rather broad and not compatible with phonon modes, which would generally sharpen with decreasing temperature, we ascribe all three absorptions to characteristic electronic interband transitions. Their resonance frequencies closely coincide with the direct transitions along the M-Γ-X directions in the reciprocal space, as predicted by band structure calculations supporting the ARPES data [19].

Figures 2(a) and (b) emphasize $\sigma_1(\omega)$ at selected temperatures in the spectral range of relevance for the following discussion. The important temperature dependence of $\sigma_1(\omega)$ implies a reshuffling of spectral weight. The insets of panels (a) and (b) in Fig. 2 deploy the integrated spectral weight ($SW(T,\omega_c) = \int_0^{\omega_c} \sigma_1(\omega,T)d\omega$, ω_c being a cut-off frequency) at 10 and 300 K in both compounds. It is clearly seen that the spectral weight is fully conserved when integrating $\sigma_1(\omega)$ at any temperatures up to $\omega_c \sim$ 2 eV, thus satisfying the optical sum rules beyond this energy [30]. There is a piling up of spectral weight at infrared frequencies upon decreasing temperature, which is more substantial in the Yb than in the Eu material. This mainly results from SW shift from the near and mid infrared spectral ranges.

In order to emphasize the comparison among the excitation spectra of both compounds, we normalize $\sigma_1(\omega)$ at 10 K by the value $\sigma_1(\omega_0)$ at the peak frequency $\omega_0 = 500$ and 2500 cm^{-1} for the Yb and Eu material, respectively, as shown in Fig. 2(c). We anticipate at this stage that the low-frequency side of the peaks at 100 and 500 cm^{-1} in the Yb compound can be fairly well approximated with a linear frequency dependence of $\sigma_1(\omega)$, a major fingerprint of this Weyl semimetal (dashed lines in Fig. 2(c) as well as thin dotted lines in Fig. 2(a)). The linearity of $\sigma_1(\omega)$ at high frequencies is very robust and not
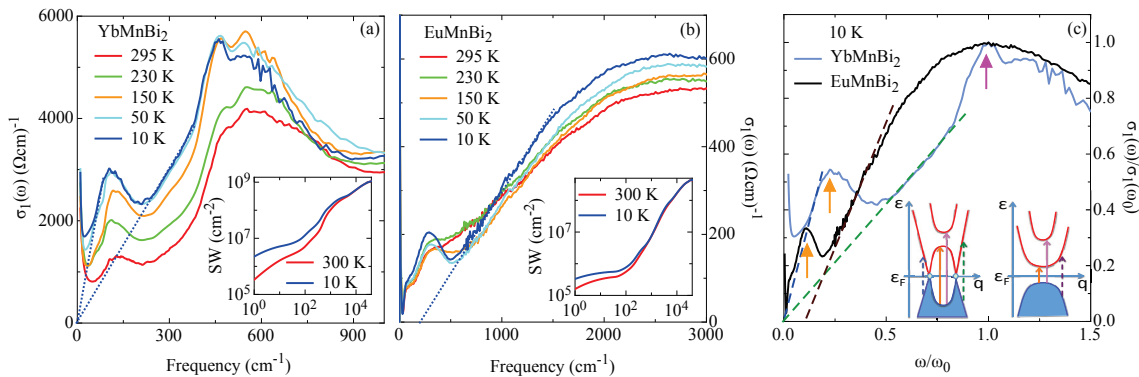
FIG. 2: (color online) (a) and (b) Temperature dependence of $\sigma_1(\omega)$ in YbMnBi$_2$ and EuMnBi$_2$, respectively, in the energy interval relevant for the present discussion. The insets display the integrated spectral weight of both compounds at 300 and 10 K with double logarithmic scales. The thin dotted lines at 10 K indicate the extrapolation to zero conductance from the quasi-linear frequency dependence in $\sigma_1(\omega)$. The cut with the frequency axis occurs at its origin only in the Yb-compound. (c) Normalized optical conductivity at 10 K with $\omega_0 = 500$ and 2500 cm^{-1} in YbMnBi$_2$ and EuMnBi$_2$, respectively. The dashed lines and plain arrows emphasize the linear frequency dependence of $\sigma_1(\omega)$ in appropriate energy intervals (see text) and the relevant excitations for both compounds, respectively. We use for plain arrows and dashed lines in the main panel, the same color code as for the plain and dashed arrows in both insets, in order to emphasize their relationships. The left inset schematically shows the band structure close to one pair of Weyl nodes (appropriate for the Yb material [19]), with the plain arrows indicating the transitions leading to the van Hove singularities in $\sigma_1(\omega)$ and the dashed ones for the transitions between states with linear dispersion leading to $\sigma_1(\omega) \sim \omega$. The right inset displays the situation of a gapped semimetal (appropriate for the Eu compound) with direct transitions (plain arrows) and transitions between states with vestige of the linear dispersion (dashed arrow) so that also $\sigma_1(\omega) \sim \omega$ (see Fig. 2 of Ref. 28, as well).

at all affected by the necessary HR extrapolation of the reflectivity for the purpose of the Kramers-Kronig transformation. This is true at all temperatures, although the energy interval of the linearity in $\sigma_1(\omega)$ gets larger at low temperatures. We have also checked that the HR extrapolation does not alter the frequency dependence of the optical conductivity at very low energy scales either, but mostly the extension of the energy interval where linearity may apply. Interestingly enough, by inspecting $\sigma_1(\omega)$ of the Yb compound in Fig. 2(a) we can convincingly state that both quasi-linear frequency dependences of the optical conductivity extrapolate to zero conductivity at the origin of the frequency axis at all temperatures. In the Eu compound, on the other hand, a linear frequency dependence of $\sigma_1(\omega)$ is unambiguously evinced at the low-frequency side of the strongest peak at 2500 cm^{-1} and most clearly at low temperatures (dashed line in Fig. 2(c) as well as thin dotted line in Fig. 2(b)). The shoulder on the low-frequency side of the peak at 300 cm^{-1} in the Eu compound (dashed arrow in Fig. 1(d), due to mostly localized itinerant charge carriers and present at all temperatures), prior the sharp onset of the metallic Drude resonance, impedes to single out a robust linearity of $\sigma_1(\omega)$ at such low frequencies, even over a tiny interval.

Band structure calculations can set the stage for the genesis of Weyl nodes and show that Dirac-like crossings, essential ingredients towards the realization of Weyl fermions, are more favorable in the staggered structure of the Yb atoms than in the coincident one of the Eu atoms relative to the Bi layers [18, 19]. The spin-orbital cou-

pling and exchange interactions lead to 'massive' Dirac states in both materials, so that gaps open in most parts of the Brillouin zone and are larger in the Eu than in the Yb compound. Furthermore, the magnetism associated with the Eu element more strongly shifts apart the electronic bands. This is overall consistent with the observation that the optical excitations in $\sigma_1(\omega)$ occur at lower energies in YbMnBi$_2$ than in EuMnBi$_2$. While EuMnBi$_2$ is a semimetal with incipient gapped Dirac cones, the degeneracy at the Dirac points in YbMnBi$_2$ is lifted by additionally breaking the time reversal symmetry with a canted antiferromagnetic order [33] of the Mn atoms, resulting in the formation of four pairs of Weyl nodes (so 8 points in total), as confirmed by ARPES investigation [19].

Given the generic features of the electronic band structure, we now turn our attention to the predicted optical conductivity in the case of two non-degenerate Dirac cones shifted in reciprocal space by a finite reciprocal q-vector [28]. The approach of Ref. 28 has been shaped for type I Weyl semimetal (i.e., it does not encounter the tilting of the Dirac cone, typical for type II) but nonetheless recognizes the overall features of the calculated electronic band structure used to support its experimental mapping by ARPES data [19]. For simplicity, the Fermi level is pinned to the location of the nodes. Beyond the intraband (Drude) contribution (which might depend very much from disorder and exact location of the Fermi level with respect to the Weyl nodes, though) the characteristic interband feature in $\sigma_1(\omega)$ should be a kink, generated by the largest absorption between the

two paired cones (orange plain arrow in left inset of Fig. 2(c)). This van Hove singularity breaks the expected linear frequency dependence of $\sigma_1(\omega)$ for a single Dirac cone in two quasi-linear parts with variable slopes (associated with transitions connecting states with linear dispersion at the Dirac cones, see blue and green dashed arrows in left inset of Fig. 2(c)). The exact behavior of the inter-band contribution to $\sigma_1(\omega)$ results from the balance between two parameters: a so-called mass term (m) related to the spin-orbital coupling and a magnetic Zeeman-like term (b) necessary to break time reversal symmetry. The resonance frequency of the van Hove singularity depends from the relative ratio m/b [28], so that for increasing m/b from 0 to 1 (where the phase boundary to a gapped semimetal is encountered) the location of the kink in $\sigma_1(\omega)$ moves toward low frequencies. For $m/b \to 1$, the two quasi-linear regions in $\sigma_1(\omega)$ are characterized by different slopes, so that the slope of the low-frequency response below the kink increases, while the photon-energy range over which it applies decreases. Above the kink, $\sigma_1(\omega)$ rises with a reduced slope with respect to the situation of the massless Dirac cone and the extrapolation of the linear $\sigma_1(\omega)$ to zero frequency cuts the conductivity axis at a finite positive value [28]. For $m/b \to 0$, $\sigma_1(\omega)$ is supposed to increase linearly with the same slope as for a single Dirac cone on both sides of the kink and the overall linear frequency dependence of $\sigma_1(\omega)$ extrapolates to zero conductance at the origin of the frequency axis. A second van Hove singularity may also occur because of transitions between states due to the lifted degeneracy of the original Dirac cones (pink plain arrow in left inset of Fig. 2(c)). For $m/b > 1$ (i.e., the case for a gapped semimetal), one may expect excitations between gapped and massive Dirac states with lifted degeneracy, intercalated by a quasi-linear frequency dependence of $\sigma_1(\omega)$ reminiscent of the incipient Dirac cones (orange and pink plain as well as brown dashed arrows in right inset of Fig. 2(c), respectively) [28].

We propose to identify the broad absorptions at 100 and 500 cm^{-1} in YbMnBi$_2$ with the predicted van Hove singularities (orange and pink plain arrows in Fig. 2(c)). Since both linear frequency dependences of $\sigma_1(\omega)$ (blue and green dashed lines and arrows in Fig 2(c)), preceding the van Hove singularities, cross zero on the conductivity axis at the frequency origin (Fig. 2(a) and (c)), we tend to believe that the magnetic term is sizable with respect to the spin-orbital contribution. Nonetheless, it remains to be explained, in contrast to the theoretical predictions [28], why the slopes differ so much among them instead to converge on one single slope as in the case for a Dirac cone. The feature with shoulder around 300 cm^{-1} and the strongest absorption at 2500 cm^{-1} in EuMnBi$_2$ identify the excitations between the gapped Dirac cones, with lifted degeneracy (orange and pink plain arrows in Fig. 2(c)). Moreover, the barely perceivable linear frequency dependence of $\sigma_1(\omega)$ (brown dashed arrow and line in Fig. 2(c)), intercalating both peaks, cuts the frequency axis away from the origin, which also hints to a

gapped, semimetallic behavior of the electronic structure in EuMnBi$_2$ [28]. Overall, our comparative study broadly images the theoretical expectations within a minimum, simplified scenario, but also calls for its extension to the case of type II Weyl semimetals, where the tilting of the single Dirac cone and the presence of broken time reversal symmetry are taken into account.
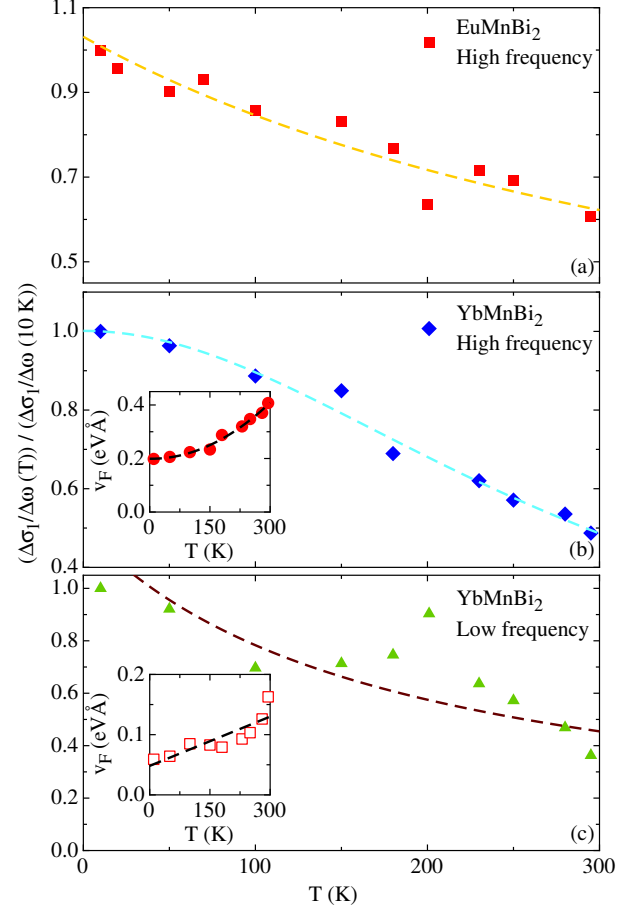

FIG. 3: (color online) Temperature dependence of the slope $\frac{\Delta\sigma_1}{\Delta\omega}$ of the linear frequency dependence in $\sigma_1(\omega)$, normalized by its value at 10 K and estimated at high and low frequencies. Here, 'high' and 'low' simply refer to the spectral ranges, where $\frac{\Delta\sigma_1}{\Delta\omega}$ was estimated (see text). The dashed lines are guide to the eyes. Insets: temperature dependence of the effective Fermi velocity (v_F) estimated from $\frac{\Delta\sigma_1}{\Delta\omega}$ of YbMnBi$_2$ at low and high frequency intervals (see Fig. 2). The dashed lines emphasize the squared (b) and almost linear (c) temperature dependence of v_F.

We now address the slope of the linear frequency dependences of $\sigma_1(\omega)$, which directly relates to the momentum-averaged slope of the dispersion relation, i.e. $< \frac{\delta E}{\delta k} > \sim \frac{\Delta\sigma_1}{\Delta\omega}$. In order to emphasize the distinct temperature dependence of $\frac{\Delta\sigma_1}{\Delta\omega}$ in different spectral ranges and for both materials, we show in Fig. 3 $\frac{\Delta\sigma_1}{\Delta\omega}$ normalized by its value at 10 K. We estimate $\frac{\Delta\sigma_1}{\Delta\omega}$ of YbMnBi$_2$ in the spectral ranges 30-70 and 200-400 cm^{-1}, which for

brevity will be denoted for the rest of the paper as 'low' and 'high' frequency range, respectively. For EuMnBi$_2$ we can confidently extract the slope at high frequencies, typically in the interval 600-1500 cm^{-1}. $\frac{\Delta\sigma_1}{\Delta\omega}$ could be eventually extracted at low frequencies too, yet on a very tiny interval (30-60 cm^{-1}), as pointed out above. At such low frequencies the slope of the linear $\sigma_1(\omega)$ of EuMnBi$_2$ is almost temperature independent, within the data scattering, and about ten times smaller than in YbMnBi$_2$ at equivalent low frequencies. Moreover, its extrapolation to zero conductance would cross the frequency axis away from its origin. In principle at this point, one can estimate the Fermi velocity (v_F) from the slope of the linear optical conductivity, as widely applied on several materials [20–24], with the formula $\sigma_1(\omega) = \frac{NG_0\omega}{24v_F}$, G_0 being the quantum conductance and N the number of Weyl nodes [34]. v_F is indeed an effective Fermi velocity within the assumption that the slope $\frac{\Delta\sigma_1}{\Delta\omega}$ calculated at finite energy intervals can be considered in the $\omega \to 0$ limit, so that $v_F \simeq \frac{NG_0}{24}(\frac{\Delta\sigma_1}{\Delta\omega})^{-1}$. The temperature dependence of v_F for YbMnBi$_2$ is shown in the insets of Fig. 2(b) and (c) [35], considering $N = 8$ [19]. From ARPES we learn that the Weyl cones are very anisotropic with v_F ranging between 0.043 and 9 eVÅ. Our optical experiment as a momentum-averaged probe does not allow any resolution in reciprocal space; in this respect our values for v_F in both ranges and at all temperatures are reasonable, yet at the lower bound of the ARPES data [19]. Our estimation may pick up the contribution by other interband transitions, not necessarily related to the Weyl cones. For instance, the low frequency tails associated with the absorptions between 1000 and 10^4 cm^{-1} in the Yb compound may definitely affect the slope of $\sigma_1(\omega)$ in the high frequency interval at the least and hence the estimation of v_F and could also explain the different v_F in both ranges. The temperature dependence of v_F seems quite intriguing, being linear for the low energy interval, despite the limited statistic due to the scattering of the data, and squared for the high one. Furthermore, v_F from the slope of $\sigma_1(\omega)$ at high energy scales doubles between 10 and 300 K. The temperature dependence of the chemical potential and of the band structure together with self-energy effects may considerably affect the joined-density-of-states, which is imaged by $\sigma_1(\omega)$, and consequently the temperature dependence of v_F as well.

With increasing temperature one may expect a decreasing occupation of electronic states below the Fermi level (E_F) accompanied by a so-called Pauli-blocking caused by thermally excited electrons above E_F. This leads to a suppression of electronic transitions in general and specifically around the Weyl points.

In conclusion, our optical results clearly characterize YbMnBi$_2$ as a Weyl semimetal and EuMnBi$_2$ as its more conventional semimetal counterpart. Even though our findings compare reasonably well with the predictions based on a generic scenario for type I Weyl semimetals [28], they equally provide evidences for subtle features in both frequency and temperature dependences of $\sigma_1(\omega)$, which may reveal peculiarities of type II Weyl semimetals. It is a challenge left for the future to develop a detailed description of their optical response, which comprehensively takes into account the full complexity of their electronic properties and magnetism.

Added Note: After resubmission we came to know the work of Ref. 36, which considers the tilting of the single Dirac cone as occurring in type II Weyl semimetal, but not yet the broken time reversal symmetry, pertinent to the title compound.

$^+$ Both authors equally contributed to the experimental work.

* Correspondence and requests for materials should be addressed to: L. Degiorgi, Laboratorium für Festkörperphysik, ETH - Zürich, 8093 Zürich, Switzerland; email: degiorgi@solid.phys.ethz.ch

[1] P. Richard et al., Phys. Rev. Lett. **104**, 137001 (2010).
[2] K.S. Novoselov et al., Nature **438**, 197 (2005).
[3] M.Z. Hasan and C.L. Kane, Rev. Mod. Phys. **82**, 3045 (2010) and references therein.
[4] H. Weyl, Z. Phys. **56**, 330 (1929).
[5] X. Wan et al., Phys. Rev. B **83**, 205101 (2011).
[6] G. Xu et al., Phys. Rev. Lett. **107**, 186806 (2011).
[7] A.A. Burkov et al., Phys. Rev. B **84**, 235126 (2011).
[8] S.-M. Huang et al., Nature Comm. **6**, 7373 (2015).
[9] S.-Y. Xu et al., Sci. Adv. **1**, 10 (2015) (doi: 10.1126/sci-adv.1501092).
[10] Y. Xu et al., Phys. Rev. Lett. **115**, 265304 (2015).
[11] A.A. Soluyanov et al., Nature **527**, 495 (2015).
[12] Z. Wang et al., Phys. Rev. Lett. **117**, 056805 (2016).
[13] L. Huang et al., Nat. Mat. (2016) (doi: 10.1038/NMAT.4685).
[14] J. Park et al., Phys. Rev. Lett. **107**, 126402 (2011).
[15] K. Wang et al., Phys. Rev. B **84**, 220401(R) (2011).
[16] K. Wang et al., Phys. Rev. B **85**, 041101 (2012).
[17] A.F. May et al., Phys. Rev. B **90**, 075109 (2014).

[18] G. Lee et al., Phys. Rev. B **87**, 245104 (2013).

[19] S. Borisenko et al., arXiv:1507.04847, unpublished (2015).

[20] R.Y. Chen et al., Phys. Rev. B **92**, 075107 (2015).

[21] A.B. Sushkov et al., Phys. Rev. B **92**, 241108(R) (2015).

[22] T. Timusk et al., Phys. Rev. B **87**, 235121 (2013).

[23] B. Xu et al., Phys. Rev. B **93**, 121110(R) (2016).

[24] D. Neubauer et al., Phys. Rev. B **93**, 121202 (2016).

[25] A. Akrap et al., Phys. Rev. Lett. **117**, 136401 (2016).

[26] P.E.C. Ashby and J.P. Carbotte, Phys. Rev. B **89**, 245121 (2014).

[27] C.J. Tabert et al., Phys. Rev. B **93**, 085426 (2016).

[28] C.J. Tabert and J.P. Carbotte, Phys. Rev. B **93**, 085442 (2016).

[29] A. Wang et al., arXiv:1604.01009, unpublished (2016).

[30] M. Dressel and G. Grüner, *Electrodynamics of Solids*, Cambridge University Press, Cambridge, England (2002).

[31] The measurement of the optical reflectivity is a bulk sensitive technique, which prevents addressing the implications of the Fermi surface arcs, as non-trivial surface states connecting the Weyl points.

[32] C.C. Homes et al., Phys. Rev. B **92**, 161109(R) (2015).

[33] As already pointed out in Ref. 19, the canted antiferromagnetic order serves the purpose to break the time-reversal symmetry, when performing band structure calculations compatible with the ARPES results. However, the real magnetic order needs still to be experimentally determined.

[34] P. Hosur et al., Phys. Rev. Lett. **108**, 046602 (2012).

[35] A similar analysis for the Eu compound in the energy interval from 600 to 1500 cm^{-1} within the assumption of $N = 8$ would lead to $v_F(T)$ values between 5.75 and 9.5 eVÅ, which gather around a linear temperature dependence, in contrast to the squared dependence observed in the Yb compound.

[36] J.P. Carbotte, Phys. Rev. B **94**, 165111 (2016).